Research Article Vol. 11, No. 2 / February 2024 / Optica 291

Ultraviolet pulse compression via cross-phase modulation in a hollow-core fiber

Yujiao Jiang,[1,2,3,6] John Pascal Messerschmidt,[1,4] Fabian Scheiba,[1,2,4] Igor Tyulnev,[1,4] Lu Wang,[1,2,4] Zhiyi Wei,[3,5] and Giulio Maria Rossi[1,2,4,*]

[1]Center for Free-Electron Laser Science CFEL, Deutsches Elektronen-Synchrotron DESY, Notkestraße 85, 22607 Hamburg, Germany
[2]The Hamburg Centre for Ultrafast Imaging, University of Hamburg, Luruper Chaussee 149, 22761 Hamburg, Germany
[3]Beijing National Laboratory for Condensed Matter Physics, Institute of Physics, Chinese Academy of Sciences, 100190 Beijing, China
[4]Physics Department, University of Hamburg, Jungiusstraße 9, 20355 Hamburg, Germany
[5]Songshan Lake Materials Laboratory, 523808 Dongguan, China
[6]yujiao.jiang@desy.de
*giulio.maria.rossi@desy.de

Received 16 November 2023; revised 16 January 2024; accepted 21 January 2024; published 13 February 2024

The generation of few-femtosecond pulses with high energy and tunable spectrum in the ultraviolet region is an ongoing challenge in ultrafast optics. Harnessing the cross-phase modulation between an intense near-infrared pulse and its third-harmonic, co-propagating in a gas-filled hollow-core fiber, we demonstrate spectral tuning, broadening, and temporal compression in the ultraviolet range. Ultraviolet pulses with negative chirp, leading to self-compression down to 6 fs during propagation in air, and energy > 10 μJ were characterized. This technique opens a way towards the realization of few-fs pulses with high energy, tunable over most of the ultraviolet range.

https://doi.org/10.1364/OPTICA.513635

1. MOTIVATION

The availability of few-fs ultraviolet (UV) pulses with μJ-level energy and tunable spectrum is particularly important for ultrafast spectroscopy, since relevant excited states of many molecules can be resonantly addressed by photons in the 200–400 nm range [1]. Tunable ultrashort UV pulses with durations down to 8.4 fs and ≈ 1 μJ energy were achieved via sum-frequency generation in a BBO crystal between two pulses obtained by different optical parametric amplifiers [2]. In order to further reduce the UV pulse duration, it is possible to exploit nonlinear processes in gases, where dispersion is much smaller compared to solids. For example, by generating the third-harmonic (THG) of a near-IR (NIR) pulse with a sub-2 cycle duration in a noble gas (inside a vacuum chamber), a UV pulse with a duration of 2.8 fs and energy of 300 nJ (after filtering out the fundamental) was obtained [3]. Optimization of the THG through the use of a laser-fabricated high-pressure gas cell allowed to achieve a record UV pulse duration of just 1.9 fs, with a pulse energy of 150 nJ [4]. This process, while enabling the shortest UV pulses, lacks spectral tunability and suffers from low conversion efficiency, which limits the available pulse energy. Recently, the resonant dispersive wave (RDW) emission process [5] was extended to large-core gas-filled hollow-core fibers (HCFs), allowing for few-fs UV pulses tunable over an impressive 110–400 nm range [6]. Temporal characterization of UV pulses obtained by RDW in neon demonstrated sub-3 fs durations over the 230–400 nm region; however, even in this case, the pulse energy is <1 μJ after filtering [7]. Earlier two-color experiments in HCF used an 800 nm pulse and its second-harmonic (400 nm) to realize $2\omega + 2\omega - \omega$ wave mixing [8], obtaining, after compression with a grating pair, 8 fs pulses centered at 270 nm with >1 μJ of energy [9]. In order to eliminate the need for lossy post compression, the scheme of chirped four-wave mixing (CFWM) was introduced and numerically explored for the generation of vacuum ultraviolet (100–200 nm) pulses [10]. Later CFWM experiments with 800 and 400 nm pulses demonstrated the generation of 270 nm pulses with 300 nJ of energy, self-compressing to 9.7 fs during propagation in air [11].

Attaining a higher UV pulse energy would not only provide access to a wider range of spectroscopic techniques, but as well to drive strong-field processes. For instance, few-fs UV pulses with energies of few tens of μJ are expected to allow for the generation of intense isolated attosecond pulses in the XUV region via high-harmonic generation, a process that is all the more efficient the shorter the wavelength used to drive it [12].

One technique that seems particularly suited for realizing higher-energy few-fs UV pulses is cross-phase modulation (XPM). XPM occurs when an intense pulse of light propagating in a Kerr medium modifies the optical phase of a second light beam, often a weaker pulse of a different color. Extensively studied in nonlinear optics [13,14], XPM is exploited in a multitude of different systems, such as quantum non-demolition measurements [15], demultiplexers of optical signals [16], and compression of ultrashort pulses [17]. The XPM process has the advantage that the

UV pulse energy can be scaled independently from the NIR pulse energy. At the same time, since in XPM the phase shift needed for broadening the UV pulse is induced by the stronger NIR pulse, the UV pulse intensity can be kept low enough to avoid any significant ionization (by scaling the HCF diameter), enabling high-energy UV pulse compression with low-energy losses. Another key advantage of XPM is that, on top of broadening the UV spectrum, it can provide extra negative dispersion to balance the positive dispersion that will be accumulated during propagation in air, leading to UV self-compression outside the HCF setup.

In this paper, we demonstrate, both experimentally and with numerical simulations (1D split-step method), the possibility to spectrally tune, broaden, and compress a high-energy UV pulse via the XPM induced by an intense NIR pulse in a neon-filled simple capillary HCF. UV pulses with duration down to 6 fs and >10 μJ of energy (measured after removing the laser fundamental) were characterized via two-dimensional spectral shearing interferometry (2DSI) [18]. These pulses, to the best of our knowledge, are 10 times more energetic than what has been shown so far for similar pulse durations in the UV range.

2. XPM SIMULATION MODEL

The XPM process was considerably studied in optical fibers and bulk materials [13,19]. Following the same approach, the nonlinear evolution of the pulse envelope $A(t, z)$ is described by the nonlinear Schrödinger Eq. (1):

$$\partial_z A = -\frac{\alpha}{2}A - \frac{ik_2}{2}\partial_\tau^2 A + \frac{k_3}{6}\partial_\tau^3 A + i\gamma(\omega)\left[|A|^2 A + \frac{i}{\omega_0}\partial_\tau\left(|A|^2 A\right)\right]. \quad (1)$$

Here α is the loss coefficient accounting for both the linear propagation losses of the EH_{11} fundamental waveguide mode, and for the small coupling losses. k_2 and k_3 are respectively the second- (GDD) and third-order dispersion terms. The k_1 term is subtracted by using the co-moving frame ($\tau = t - k_1 z$). The two nonlinear terms in this equation are self-phase modulation (SPM) and self-steepening. Here γ is given by $\gamma(\omega) = n_2\omega/(cA_{\text{eff}})$, where n_2 is the nonlinear refractive index, A_{eff} is the effective mode area, ω is the carrier frequency, and c is the speed of light in vacuum.

For XPM we consider a NIR pulse E_1, centered at 800 nm, and its third-harmonic E_2, centered at 267 nm. Other third-order nonlinear processes, such as sum-frequency and third-harmonic generation, are omitted since they are not phase-matched. The resulting nonlinear frequency shifts for both pulses are given by

$$\partial_\tau \phi_1^{\text{NL}} = -n_2\frac{\omega_1}{c}\left(\partial_\tau|A_1|^2 + 2\partial_\tau|A_2|^2\right)z, \quad (2)$$

$$\partial_\tau \phi_2^{\text{NL}} = -n_2\frac{\omega_2}{c}\left(\partial_\tau|A_2|^2 + 2\partial_\tau|A_1|^2\right)z. \quad (3)$$

The XPM effect on the UV pulse is $2(\partial_\tau|A_1|^2)/(\partial_\tau|A_2|^2)$ times stronger than its own SPM. By choosing $|A_1| \gg |A_2|$ the UV broadening is dominated by XPM, and ultrabroadband spectra can be achieved for intensities well below the ionization threshold.

Figure 1 gives a qualitative description of the XPM process depending on delay among the interacting pulses. When the UV pulse overlaps with the leading edge of the NIR pulse it is broadened towards longer wavelengths; on the contrary when it overlaps with the trailing edge it is broadened towards shorter wavelengths. At the peak of the NIR pulse the broadening occurs in both directions. By looking at the time derivative of the NIR envelope (shown in blue) we can recognize the regions of negative dispersion

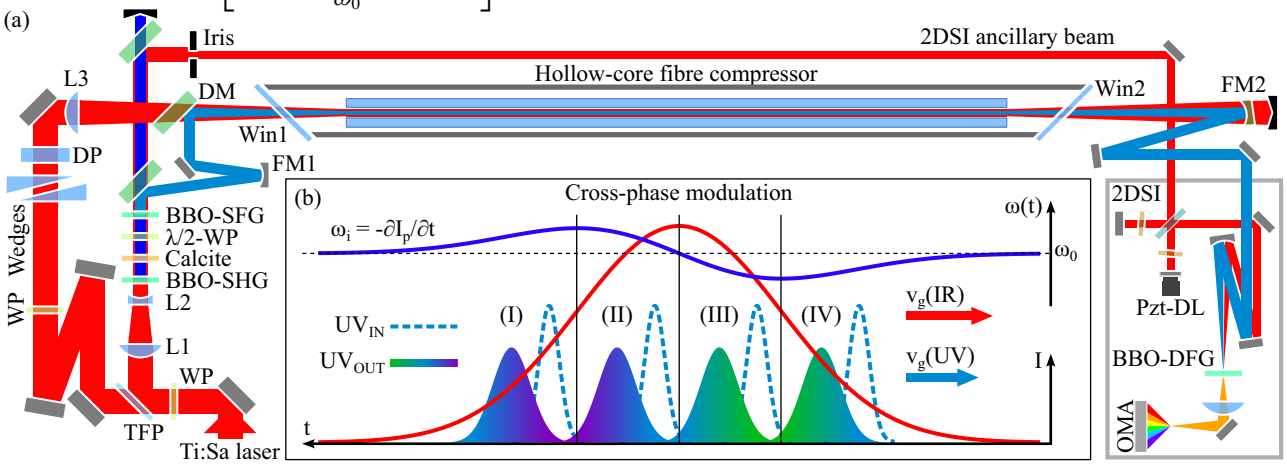

Fig. 1. (a) Schematic of the experimental setup. The input NIR beam is split into two arms via a thin film polarizer (WP + TFP). In the right arm, the fundamental beam diameter is reduced (telescope L1, L2) and frequency-tripled via the combined action of a 100 μm thick second-harmonic generation Type-I crystal (BBO-SHG), a birefringent delay plate (calcite), a zero-order dual wavelength wave plate (λ/2-WP, λ/2 at 800 nm + λ at 400 nm), and a 50 μm thick sum-frequency generation Type-I crystal (BBO-SFG). Dielectric mirrors are used to isolate the third-harmonic and focus it (FM1). In the left arm, the laser fundamental is delayed to match the UV generation arm (fine tuning by wedge insertion). A thick glass plate (DP) is used to adjust the near-IR pulse duration independently from the UV arm and a lens (L3) is used to focus at the same position as the UV beam. The two pulses are overlapped with parallel polarization via a dichroic mirror (DM) and launched in the HCF. At the HCF output the broadened UV pulse is separated from the near-IR beam and guided through the 2DSI pulse measurement setup, where a small portion of laser fundamental is used to produce the ancillary pulses. (b) The central panel shows the effect of XPM on the UV pulse. Depending on the initial delay of the UV pulse (dashed blue envelope) with respect to the NIR pulse (red envelope), the UV broadened pulse (solid color gradient) will have different characteristics: (I) and (II) are upshifted while (III) and (IV) are downshifted; (I) and (IV) have negative chirp while (II) and (III) have positive chirp.

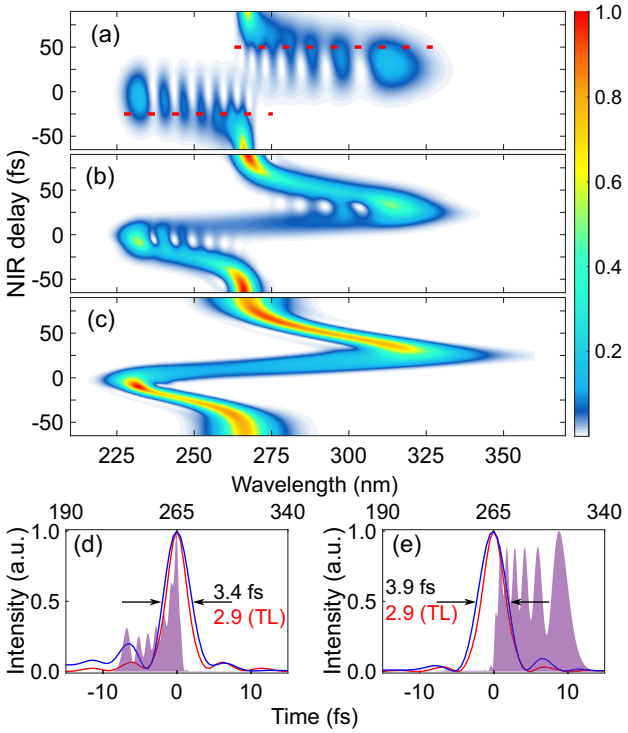

Fig. 2. Simulated UV XPM spectrum during NIR delay scans for different input UV pulse durations (TL) equal to (a) 40 fs, (b) 20 fs, and (c) 10 fs. The HCF length was set to 1 m and a fixed NIR pulse duration (TL) of 40 fs. (d), (e) Upshifted and downshifted UV pulses obtained for NIR delays of −30 fs and 50 fs, respectively (red dashed lines), for the case in (a), together with their corresponding spectra (in purple). FWHM durations of 3.4 and 3.9 fs were obtained by numerically propagating through (d) 140 μm and (e) 350 μm of MgF_2.

(GDD $<$ 0) that we want to exploit for self-compression, corresponding to the first half of the leading edge and the last half of the trailing edge (IV and I in Fig. 1).

Based on Eq. (1), we performed numerical simulations of the UV spectrum broadening depending on the initial delay of the NIR pulse (Fig. 2). Different initial UV pulse durations (40, 20, and 10 fs) were simulated, while keeping the NIR pulse duration fixed (40 fs, transform limited). The pulse energies were 1.6 mJ and 20 μJ for the NIR and UV, respectively. We chose a 1 m long fused-silica HCF (see Supplement 1) with a core diameter of 250 μm, filled with 1.5 bar of neon. In order to precisely simulate the propagation of the UV pulse, we propagated the full phases and subtracted the linear phase of E_1, the co-moving frame of the NIR pulse, instead of fitting its dispersion with Tailor coefficients.

The strongest UV broadening in the negative GDD regions occurs when the two pulses have similar duration [Fig. 2(a)]. Here, durations down to 3.9 fs for the downshifted and 3.4 fs for the upshifted pulses can be achieved after propagation in MgF_2 and/or air [Figs. 2(d) and 2(e)]. For UV input pulse durations significantly shorter than the NIR [Figs. 2(b) and 2(c)], if the UV overlaps with the tails of the NIR, the XPM, instead of broadening, predominantly down/up shifts the whole spectrum. When the pulses overlap (NIR delay ∼0), the UV spectrum reaches the maximum broadening, however with a complicated spectral phase.

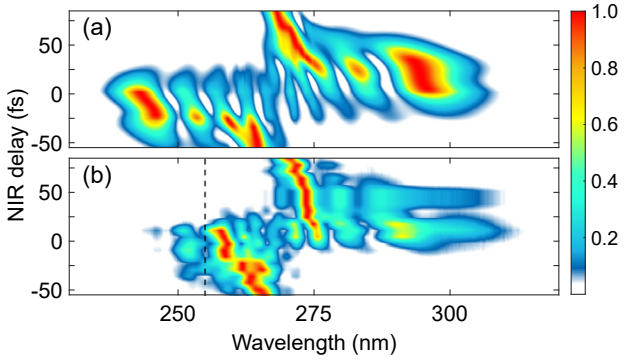

Fig. 3. (a) Simulated and (b) experimental NIR delay scans for input pulse durations $\tau_{UV} = 48$ fs (positively chirped) and $\tau_{NIR} = 45$ fs (close to TL). Pulse durations were characterized via 2DSI and SHG-FROG. The dashed line in (b) marks the cutoff wavelength of dielectric mirror reflectivity.

3. EXPERIMENT AND SIMULATION RESULTS

In Fig. 1 we present the experimental setup. We used up to 2.5 mJ, ∼40 fs pulses centered at 800 nm, originating from a 3 kHz Ti:sapphire amplifier. At the input of the setup, the fundamental pulse is split into two arms, one dedicated to the UV generation (third-harmonic) and one used to drive the XPM. The UV pulse duration was adjusted in 20–48 fs range by changing its chirp with the compressor after the laser amplifier. The NIR pulse is kept nearly transform limited (after Win1) by choosing a proper dispersive plate (DP) placed before the focusing lens (L3). At the input of the HCF, 1 m long, with 250 μm core diameter and filled with 1.7–1.8 bar of neon, the fundamental pulse had 1.6 mJ of energy (70% transmission through the HCF), while the UV pulse energy was adjusted in the 20–28 μJ range, depending on its duration. The UV transmission through the HCF ranged from 53% to 73%, depending on daily alignment. The UV pulse energy was kept well below 50 μJ, since at this pulse energy we observed a fast degradation of the fused-silica fiber, a corresponding drop of transmission to about 23%, and consequently a reduced spectral broadening. When the UV pulse strongly overlaps with the NIR peak (NIR delay ∼0 fs), the UV output energy drops significantly due to excessive ionization.

To verify the accuracy of the model, in the first experiment we compared the UV spectral broadening measured during a NIR delay scan with a numerical simulation that used actual pulse characterization data for both the UV and the NIR pulses [Figs. 3(b) and 3(a)]. The substantial agreement between theory and experiment validates our numerical model. Unfortunately the region below 260 nm could not be measured due to the drop in the reflectivity of the multi-layer mirrors (Eksma 082-2840-i0-45) used to separate the UV from the NIR after broadening. The use of these "standard" mirrors limits the possibility of characterization to downshifted pulses only. In fact, in order to separate the upshifted UV pulses from the NIR, different high-reflectivity mirrors, covering the 220–270 nm region, are needed.

In a second experiment, we characterized the UV pulse duration by implementing a 2DSI setup based on difference frequency generation (DFG) [20]. Here the UV pulse is down-converted in a BBO crystal by means of two narrowband components (called ancillary pulses), spectrally separated by just 6 nm, obtained by filtering the laser fundamental spectrum (scheme in Fig. 1). These two down-converted replicas spectrally overlap and interfere. The

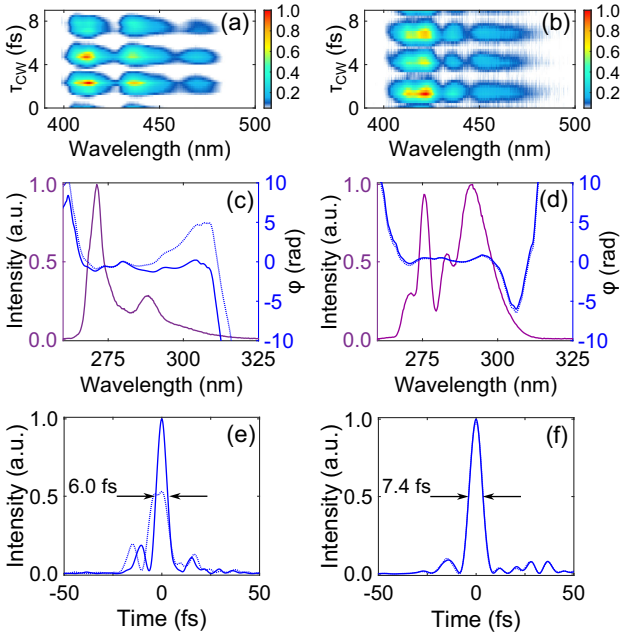

Fig. 4. UV pulse characterization after XPM. In this experiment, the input pulse durations were $\tau_{UV} = 38$ fs (positively chirped, ~20 fs TL) and $\tau_{NIR} = 42$ fs (close to TL). The 2DSI measurements of the output UV were done for (a) NIR delay equal to ~65 fs and (b) NIR delay ~56 fs. (c), (d) Corresponding measured UV spectra and spectral phases at the 2DSI measurement point (dashed lines) and after adding/subtracting a suitable amount of air propagation (solid lines). Corresponding temporal profiles of the UV pulses showing (e) FWHM duration of 11.2 fs at the measurement point (dashed line) and 6.0 fs after removing 28 cm of air propagation (solid line) and (f) duration of 7.5 fs at the measurement point (dashed line) and 7.4 fs after adding 4.1 cm of air propagation (solid line). The 2DSI measurement point is located ~1.3 m after the output window of the HCF setup (Win2).

spectral phase of the UV pulse is obtained by collecting the down-converted signals via a visible-range spectrometer while scanning the delay (or relative phase) among the two ancillary pulses [τ_{CW} in Figs. 4(a) and 4(b)]. In the experiment, the broadened UV pulses were propagating for about 1.3 m after the output window of the HCF (Win2, 100 μm of MgF_2) before reaching the BBO crystal of the 2DSI setup. Therefore the UV pulses acquire additional dispersion during the propagation in air.

We performed pulse characterization for two different input NIR delays, and compared them with simulations. When the input NIR delay is set around 65 fs (obtained by comparison with simulations), the UV pulse mostly interacts with the first half of the leading edge of NIR pulse, and its spectrum is mildly downshifted. The corresponding pulse characterization [Figs. 4(a), 4(c), and 4(e)] showed that, in this case, the UV pulse self-compressed to 6.0 fs, after 1 m of air propagation past Win2. Therefore, at the measurement position, the UV was slightly positively chirped to 11.2 fs FWHM. After decreasing the NIR delay to about 56 fs, the UV pulse broadening and down shifting increase. In this case the UV pulse acquired sufficient negative chirp, to balance the dispersion of Win2 and the full 1.3 m air propagation. This resulted in an almost flat spectral phase at the measurement position; see Fig. 4(d), corresponding to 7.5 fs, which could be further reduced to 7.4 fs if an additional 4.1 cm of air propagation would be added. The measured output UV pulse energy in both cases was 11 μJ, corresponding to an overall transmission of >50%.

We performed another numerical simulation with input UV and NIR pulse parameters identical to those used during the pulse characterization experiments. It should be noted that the input UV pulses were shorter (although slightly chirped) with respect to the NIR delay scan experiment in Fig. 3. Figure 5 shows the calculated temporal profiles of the UV pulses after broadening as a function of the initial NIR delay. Here, after the HCF, we numerically propagate the pulses through 100 μm MgF_2 and 28.4 cm of air. The broadened spectra calculated for NIR delays of 65 and 56 fs [Figs. 5(b) and 5(c)] are in good agreement with the ones experimentally measured [Figs. 4(c) and 4(d)]. However, simulated temporal profiles are somewhat shorter then those measured experimentally. A possible explanation is that, in the 2DSI measurements, the DFG could not be perfectly phase-matched over the entire UV spectrum due to the ~10 μm thickness of the BBO crystal (see Supplement 1). This could cause the measured pulse duration to be slightly overestimated. A 5 μm BBO crystal would allow for broader phase-matching, extending the characterization UV pulses down to ~3 fs. Moreover, the simulated pulses have less negative GDD than the measured ones and self-compress after a shorter propagation outside the HCF setup. The additional negative GDD found in experiments could come from the HCF dispersion, which was neglected in the 1D simulation. We also note that for the case of NIR delay = 65 fs [Figs. 4(c), 4(e)/Fig. 5(b)], the simulation matches the experimental data better than for NIR delay = 56 fs [Figs. 4(d), 4(f)/Fig. 5(c)]. This is attributable to the use, in our simulations, of the ADK ionization model, which is known to underestimate the ionization rate for intensities in the TW-range [21]. The discrepancy in the ionization rate is more relevant to the case in Figs. 4(d), 4(f)/Fig. 5(c), as here the NIR and UV pulses overlap more, not only causing a higher intensity (and thus more plasma), but also allowing the UV to participate in ionization. This causes ionization to shift towards the multi-photon regime and thus increases the discrepancy with the ADK tunneling model. A larger amount of plasma can also explain the pronounced

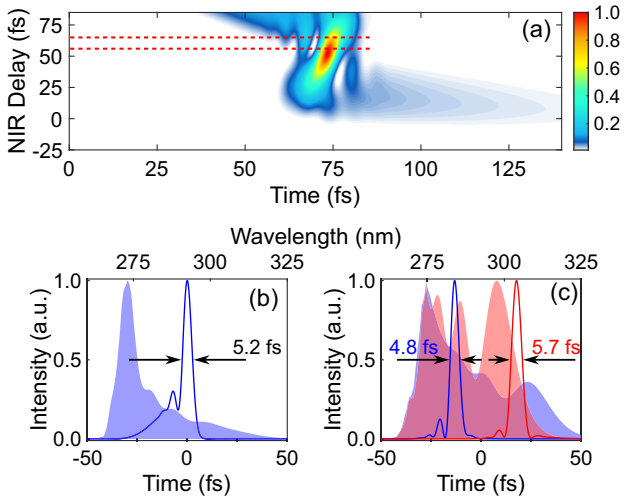

Fig. 5. (a) Simulated UV pulses after XPM during a NIR delay scan for the same input pulse parameter as in the experiment shown in Fig. 4. After XPM in the HCF the pulses are numerically propagated through 100 μm of MgF_2 and 28.4 cm of air. Spectra and temporal profiles corresponding to NIR delays of (b) 65 fs and (c) 56 fs (blue color). Here, after the 100 μm MgF_2 window, the air propagation distance was individually optimized to give the shorter duration [12.3 cm of air in (b), 28.4 cm in (c)]. The red spectrum and pulse in (c) are simulated while considering an ionization rate $w = 80 \cdot w_{ADK}$.

blue-shift of the experimental spectrum, compared to the simulated one. To verify this, we performed another simulation for NIR delay = 56 fs, this time assuming ionization rates 80 times higher than obtained by the ADK formula ($w = 80 \cdot w_{ADK}$). In this case, the broadened UV spectrum and the corresponding compressed pulse, shown in red in Fig. 5(c), show a much better agreement with experimental data.

4. DISCUSSION AND OUTLOOK

UV pulse broadening via XPM in a HCF has several key advantages. First, in neon it allows the input UV pulse spectrum to be broadened by a factor of ∼10, thus enabling TL durations down to 3.5 fs, with a throughput efficiency ≥ 50%. By controlling the delay among the two interacting pulses it is also possible to tune the central wavelength of the UV pulse, although ultra-wide spectra with negative GDD can only be obtained at two positions, corresponding to central wavelengths of ∼250 nm and ∼290 nm. To further extend to shorter wavelengths, it might be possible to use as input UV pulse the fourth-harmonic (200 nm) instead of the third (see Supplement 1, Fig. S11). Another important aspect of XPM is that, thanks to the possibility of obtaining pulses with GDD < 0 at the HCF output, the broadened UV pulses reach their minimum duration after a certain propagation, e.g., a few hundred μm in MgF_2 or a few tens of cm in air. Remarkably, this technique makes it possible to obtain an order of magnitude higher pulse energy at the sample position than previously reported for sub-8 fs UV pulses. It should also be possible to scale up the energy further by using a HCF with a larger core. For example, a HCF with a core diameter of 500 μm should support an UV input energy of up to ∼100 μJ, thus enabling 6 fs UV pulses with energy > 50 μJ.

In order to further reduce the pulse duration and reach the few-fs range, few paths could be followed. One way is to increase the XPM interaction length by means of a longer HCF and a longer NIR pulse (with the same intensity). Alternatively a gas with a larger nonlinear refractive index can be used. In Fig. 6 is shown a broadband UV spectrum supporting a 2.4 fs TL duration that we obtained via XPM in an argon-filled HCF. Such pulses, according to simulations, self-compress to ∼3 fs after a short propagation (see Supplement 1). Another interesting direction to reduce the UV pulse duration is to shape the envelope of the NIR pulse in the form of an M, as proposed in [14]. In this case, if the UV pulse overlaps with the central region (valley) of the NIR, it is symmetrically broadened (both upshifted and downshifted) while still acquiring negative dispersion. To preserve such a short pulse duration, it is no longer possible to use high-reflectivity dielectric mirrors to separate the UV from the fundamental (due to oscillations in the GD). In this case it is necessary to use a Fresnel reflection, for instance, from a silicon plate, which, despite involving much higher losses for the UV (∼80%), would support few-fs pulses with several μJ energy.

Funding. Cluster of Excellence 'CUI: Advanced Imaging of Matter' of the Deutsche Forschungsgemeinschaft (DFG)-EXC 2056-project ID 390715994; Deutsches Elektronen-Synchrotron.

Acknowledgment. During the relevant period, Yujiao Jiang was holding a fellowship from the "Helmholtz–OCPC Postdoc Program."

Disclosures. The authors declare no conflicts of interest.

Data availability. Data underlying the results presented in this paper are available in [22].

Supplemental document. See Supplement 1 for supporting content.

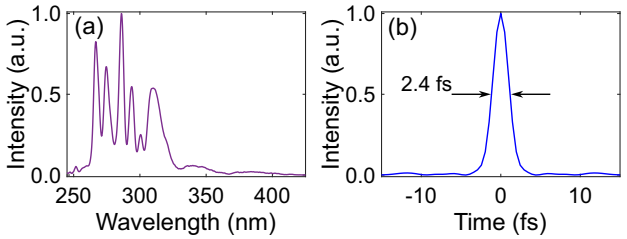

Fig. 6. (a) Experimental spectrum of the UV pulse after broadening (downshifted) via XPM in a HCF filled with 0.6 bar of argon and (b) corresponding TL pulse.

REFERENCES

1. M. Chergui, "Ultrafast molecular photophysics in the deep-ultraviolet," J. Chem. Phys. **150**, 070901 (2019).
2. R. B. Varillas, A. Candeo, D. Viola, *et al.*, "Microjoule-level, tunable sub-10 fs UV pulses by broadband sum-frequency generation," Opt. Lett. **39**, 3849–3852 (2014).
3. F. Reiter, U. Graf, M. Schultze, *et al.*, "Generation of sub-3 fs pulses in the deep ultraviolet," Opt. Lett. **35**, 2248–2250 (2010).
4. M. Galli, V. Wanie, D. P. Lopes, *et al.*, "Generation of deep ultraviolet sub-2-fs pulses," Opt. Lett. **44**, 1308–1311 (2019).
5. S.-J. Im, A. Husakou, and J. Herrmann, "High-power soliton-induced supercontinuum generation and tunable sub-10-fs VUV pulses from kagome-lattice HC-PCFs," Opt. Express **18**, 5367–5374 (2010).
6. J. C. Travers, T. F. Grigorova, C. Brahms, *et al.*, "High-energy pulse self-compression and ultraviolet generation through soliton dynamics in hollow capillary fibers," Nat. Photonics **13**, 547–554 (2019).
7. M. Reduzzi, M. Pini, L. Mai, *et al.*, "Direct temporal characterization of sub-3-fs deep UV pulses generated by resonant dispersive wave emission," Opt. Express **31**, 26854–26864 (2023).
8. C. G. Durfee, S. Backus, M. M. Murnane, *et al.*, "Ultrabroadband phase-matched optical parametric generation in the ultraviolet by use of guided waves," Opt. Lett. **22**, 1565–1567 (1997).
9. C. G. Durfee, S. Backus, H. C. Kapteyn, *et al.*, "Intense 8-fs pulse generation in the deep ultraviolet," Opt. Lett. **24**, 697–699 (1999).
10. I. Babushkin and J. Herrmann, "High energy sub-10 fs pulse generation in vacuum ultraviolet using chirped four wave mixing in hollow waveguides," Opt. Express **16**, 17774–17779 (2008).
11. Y. Kida, J. Liu, T. Teramoto, *et al.*, "Sub-10 fs deep-ultraviolet pulses generated by chirped-pulse four-wave mixing," Opt. Lett. **35**, 1807–1809 (2010).
12. T. Severt, J. Troß, G. Kolliopoulos, *et al.*, "Enhancing high-order harmonic generation by controlling the diffusion of the electron wave packet," Optica **8**, 1113–1121 (2021).
13. G. P. Agrawal, P. L. Baldeck, and R. R. Alfano, "Temporal and spectral effects of cross-phase modulation on copropagating ultrashort pulses in optical fibers," Phys. Rev. A **40**, 5063–5072 (1989).
14. M. Spanner, M. Y. Ivanov, V. Kalosha, *et al.*, "Tunable optimal compression of ultrabroadband pulses by cross-phase modulation," Opt. Lett. **28**, 749–751 (2003).
15. P. Grangier, J. Levenson, and J. P. Poizat, "Quantum non-demolition measurements in optics," Nature **396**, 537–542 (1998).
16. B.-E. Olsson and D. Blumenthal, "All-optical demultiplexing using fiber cross-phase modulation and optical filtering," IEEE Photon. Technol. Lett. **13**, 875–877 (2001).
17. Q. Z. Wang, P. P. Ho, and R. R. Alfano, "Degenerate cross-phase modulation for pulse compression and amplification of ultrashort laser pulses," Opt. Lett. **15**, 1023–1025 (1990).
18. J. R. Birge, R. Ell, and F. X. Kärtner, "Two-dimensional spectral shearing interferometry for few-cycle pulse characterization," Opt. Lett. **31**, 2063–2065 (2006).
19. P. Baldeck, P. Ho, and R. Alfano, *Cross-phase Modulation: A New Technique for Controlling the Spectral, Temporal, and Spatial Properties of Ultrashort Pulses* (Springer, 1989).
20. R. Borrego-Varillas, A. Oriana, F. Branchi, *et al.*, "Optimized ancillae generation for ultra-broadband two-dimensional spectral-shearing interferometry," J. Opt. Soc. Am. B **32**, 1851–1855 (2015).

21. Y. H. Lai, J. Xu, U. B. Szafruga, *et al.*, "Experimental investigation of strong-field-ionization theories for laser fields from visible to midinfrared frequencies," Phys. Rev. A **96**, 063417 (2017).

22. Y. Jiang, J. P. Messerschmidt, F. Scheiba, *et al.*, "Ultraviolet pulse compression via cross-phase modulation in a hollow-core fiber," Zenodo, 2024, https://doi.org/10.5281/zenodo.10554724.